Continental configuration controls ocean oxygenation

2	during the Phanerozoic
3	
4	Alexandre POHL ^{1,2*} , Andy RIDGWELL ^{1*} , Richard G. STOCKEY ³ , Christophe
5	THOMAZO ^{2,4} , Andrew KEANE ⁵ , Emmanuelle VENNIN ² , Christopher R. SCOTESE ⁶
6	¹ Department of Earth and Planetary Sciences, University of California, Riverside, CA,
7	USA
8	² Biogéosciences, UMR 6282, UBFC/CNRS, Université Bourgogne Franche-Comté, 6
9	boulevard Gabriel, F-21000 Dijon, France
10	³ Department of Geological Sciences, Stanford University, Stanford, CA 94305, USA
11	⁴ Institut Universitaire de France, Paris, France
12	⁵ School of Mathematical Sciences and Environmental Research Institute, University
13	College Cork, Cork, Ireland
14	⁶ Department of Earth and Planetary Sciences, Northwestern University, Evanston,
15	Illinois 60208, USA
16	
17	*These authors contributed equally to this work
18	
19	

ABSTRACT

21

22

23

24

25

26

27

28

29

30

31

32

33

34

35

36

The early evolutionary and much of the extinction history of marine animals, is thought to be driven by changes in dissolved oxygen concentrations ($[O_2]$) in the ocean $^{1-3}$. In turn, [O₂] is widely assumed to be dominated by the geological history of atmospheric oxygen $(pO_2)^{4,5}$. Here, in contrast, we show via a series of Earth system model experiments how continental rearrangement during the Phanerozoic drives profound variations in ocean oxygenation and induces a fundamental decoupling in time between upper-ocean and benthic [O₂]. We further identify the presence of state transitions in the global ocean circulation, which lead to extensive deep-ocean anoxia developing in the early Phanerozoic even under modern pO₂. The occurrence of stable kyr-scale oscillations in ocean oxygenation that we find also provides a causal mechanism that might explain elevated rates of metazoan radiation and extinction during the early Paleozoic⁶. The absence, in our modelling, of any simple correlation between global climate and ocean ventilation, and the occurrence of profound variations in ocean oxygenation independent of atmospheric pO_2 , presents a challenge to the interpretation of marine redox proxies, but also points to a hitherto unrecognized role for continental configuration in the evolution of the biosphere.

38

39

40

41

42

43

44

45

46

37

MAIN TEXT

The availability of dissolved oxygen in the ocean exerts a critical control on habitability for marine animals^{1,7} and is thought to have dramatically impacted their evolution from the late Neoproterozoic and through the Phanerozoic Eon (541-0 Ma)¹⁻³. Indeed, the emergence of the first unambiguous metazoans during the Ediacaran period (635–541 Ma) may have been triggered by the occurrence of ambient [O₂] sufficient to support the metabolism of a large body size¹. Further increases in ocean oxygenation may have contributed to the Great

Ordovician Biodiversification Event⁸ as well as the rise of large predatory fish in the Devonian⁹. Conversely, episodic deoxygenation is considered the primary kill mechanism during many of the major Phanerozoic mass extinction events, including the Late Ordovician¹⁰, Late Devonian¹¹ and end Permian⁷.

The past few decades have seen the development and application of a variety of geochemical redox proxies such as δ²³⁸U¹², δ⁹⁸Mo⁹, I/Ca¹³ and iron speciation¹⁴, which have provided us with unprecedented insights into the Phanerozoic history of ocean oxygenation^{5,13}. In parallel, numerical models have been instrumental in helping interpret the proxy trends and test hypotheses for the underlying driving mechanisms^{4,15}. Principal amongst the ideas that have arisen is that changes in atmospheric *p*O₂ can be inferred from the ocean^{4,5,15}. However, for computational reasons, this link between ocean [O₂] and atmospheric *p*O₂ has invariably been made without considering how ocean circulation may have changed through time^{4,5,15}. While the importance of continental configuration for ocean circulation and surface climate has started to be studied systematically^{16–18}, spatial patterns of ocean geochemistry and redox have only been considered in a limited number of continental configurations (e.g. refs^{7,19}) and often analyzed in temporal isolation. Here we explicitly address this gap, employing an Earth System Model of intermediate complexity to quantify how continental configuration can modulate the distribution of [O₂] in the ocean, thereby leading us to a radically different conclusion regarding the inferences that can be drawn from marine redox proxy records.

We base our analysis on a series of past ocean circulation scenarios generated using cGENIE²⁰, an Earth System Model of intermediate complexity designed to simulate the large-scale biogeochemical cycles and patterns in the ocean, and one that has previously been shown to be capable of simulating regional-scale distributions of [O₂] in the present-day ocean²⁰ as well as in the geological past^{19,21} (see Methods, Extended Data Fig. 1). In these experiments, we consider both the potential role of changing ecological structure in the ocean

(using the size-structured plankton model of ref²²) as well as the influence of temperature on metabolic rates (following ref²³) in creating 3D realizations of the potential distribution of [O₂] in the ocean. Based on the continental reconstructions of Scotese and Wright²⁴, we conducted one simulation every 20 Myrs through the Phanerozoic, for a total of 28 simulated time slices. In order to help isolate the impact of continental configuration from other changes occurring through the Phanerozoic, only the continental configuration²⁴ (plus physical atmospheric boundary conditions – see Methods) was varied from one time slice to the other. Solar luminosity (1368 W m⁻²), atmospheric oxygen concentration (20.95 %), and ocean nutrient inventory (2.1 μmol kg⁻¹ PO₄) were kept identical in every model run, and in a first series of simulations (#1), we also kept atmospheric *p*CO₂ fixed (at 2240 ppm, see Methods). We hence are not aiming to reconstruct the Phanerozoic evolution of climate here (see e.g. refs^{16,18}), nor necessarily provide a reconstruction of past [O₂] in the ocean or even recover modern distributions with high fidelity, but rather, expose the specific impact of changes in continental configuration on gross ocean oxygenation.

Despite assuming both invariant solar constant and pCO_2 , substantive variability in climate through the Phanerozoic occurs in the model (Fig. 1b). This is an expected result of sea-level driven changes in the proportion of absorptive ocean surface vs. more reflective land surface^{17,25} as well as of continental latitudinal distribution, and in a principal component analysis conducted across all 28 time slices we find a strong positive correlation between global mean sea-surface temperature (SST) and global ocean surface area (Fig. 1e; $R^2 = 0.585$). Given our assumption of invariant pO_2 (deliberately chosen to expose the role of the continental configuration), we find a relatively straightforward and expected inverse relationship between mean ocean surface [O₂] and SST (Fig. 1b, e) – driven primarily via changes in oxygen solubility and modulated by the latitudinal distribution of ocean surface area. Global mean subsurface (ca. 90–190 m depth in the model) [O₂] exhibits a more

exaggerated temporal evolution (Fig. 1c). Respiration of organic matter exported from the ocean surface now strongly amplifies subsurface oxygen variability (Fig. 1c, e) and introduces new features unconnected to SST changes, such as the ~35 µmol kg⁻¹ decrease from 460 to 400 Ma. This is our first hint of the importance of changing continental distribution and hence large-scale pattern of ocean circulation, which in the case of subsurface [O₂] is via changes in the resupply of nutrients to the surface. Even without attempting to simulate a realistic sequence of Phanerozoic climate states (and hence changing ocean surface oxygen solubility), our modelling provides hints as to the timing of Oceanic Anoxic Events (OAEs) during the Phanerozoic (Fig. 2, Extended Data Fig. 2). For instance, seafloor ocean deoxygenation develops in the paleo-Tethys during the Permian-Triassic transition (ca. 260 Ma)²⁶ and in the central Atlantic during the Early Cretaceous (ca. 120 Ma)²⁷ and Late Cretaceous (ca. 100 Ma)²⁸. That the Late Devonian OAE (380 Ma)²⁹ and Toarcian OAE (ca. 180 Ma)³⁰ are not captured by our simulations may be a result of the coarse model grid (for the Tethys Ocean during the Toarcian OAE in particular³⁰; Fig. 2, Extended Data Fig. 2). This could also be interpreted as reflecting the need for a strong perturbation (warming and nutrient-driven increase in primary productivity) at that time to trigger an OAE, since the continental configuration itself is not particularly prone to ocean deoxygenation in our model simulations.

97

98

99

100

101

102

103

104

105

106

107

108

109

110

111

112

113

114

115

116

117

118

119

120

121

Our unexpected discovery from the numerical modelling is how variable global deepocean [O₂] (calculated as the mean of all benthic grid points in the model below 1000 m depth) is (Fig. 1d); ranging from 30 μ mol kg⁻¹ (and near fully anoxic) to 178 μ mol kg⁻¹ (a little higher than modern). The early Paleozoic (541 to 460 Ma) in particular stands out, and is characterized by anomalously poor deep seafloor oxygenation (generally < 45 μ mol kg⁻¹) in the model, with an abrupt rise to 171 μ mol kg⁻¹ at 440 Ma and thereafter mostly remaining above 100 μ mol kg⁻¹ (Fig. 1d). The step change in benthic oxygenation simulated between

460 Ma and 440 Ma is similarly observed using an alternative set of continental reconstructions³¹ (Extended Data Fig. 4). Simulated water age (the mean time since a water parcel was last exposed to the atmosphere) anti-correlates with mean global and benthic $[O_2]$ (Fig. 1d, e), while SST and global water age do not correlate (Fig. 1e; $R^2 = 0.001$), pointing to the dominance of a paleogeographical control on deep-ocean oxygenation.

To further simplify the attribution of causes of benthic [O₂] variability through the Phanerozoic and eliminate global climate change and resulting solubility-driven upper-ocean [O₂] variations as explanatory factors, we carried out a second series of model experiments (#2) in which we kept mean global SST and surface oxygenation largely invariant (Fig. 3). Climate detrending was achieved by varying *p*CO₂ in the model. Variance in mean benthic [O₂] (Fig. 3d) is now if anything, even greater than in #1 (Fig. 1d) and the general trend of a poorly oxygenated early Paleozoic deep ocean still stands. These results confirm that benthic anoxia in the early Paleozoic ocean results from changes in the deep-ocean circulation in the model, rather than temperature-driven variations in upper-ocean [O₂]. Sensitivity tests demonstrate that global mean temporal trends and spatial oxygenation patterns are largely independent of whether a temperature-dependent (Fig. 1) or fixed remineralization profile (Extended Data Fig. 5) is assumed. Similarly, patterns of benthic [O₂] are only weakly impacted by uncertainties in the position of mid-ocean ridges (Extended Data Figs. 6, 7).

The role of continental configuration in creating conditions of extreme deep-ocean deoxygenation and weakened ventilation (old water mass ages) during the early Paleozoic (prior to 440 Ma in series #1 (Fig. 1d), and prior to 420 Ma in series #2 (Fig. 3d)), arises from the existence of state transitions in the large-scale circulation of the ocean in the model. Using series #1 as an example, the oldest time slices (540 – 500 Ma) are characterized by a poorly ventilated seafloor with deep waters forming over the South Pole (Figs. 1d and 2, Extended Data Fig. 8a). At 480 and 460 Ma, the ocean circulation oscillates between the

previous poorly-ventilated state and a better-ventilated state, the latter state subsequently becoming stabilized at 440 Ma by further tectonic rearrangement (Figs. 1d and 2, Extended Data Fig. 8a). Of course, the differences in the two simulation series illustrate that the climate state also influences the ocean circulation regimes (contrast Figs. 1 and 3; see also Extended Data Figs. 8 and 9). Several lines of evidence suggest that these state transitions are a robust characteristic of the early Paleozoic, at least in the cGENIE model. Indeed, additional simulations conducted using idealized land-sea masks reveal that these state transitions may be a characteristic feature of continental configurations with one pole free of land (Extended Data Fig. 10; Methods), such as the one of the early Paleozoic (Fig. 2), and a similar reorganization of the global ocean circulation has previously been shown to best explain the expansion of seafloor anoxia during Late Ordovician glaciation (Extended Data Fig. 10 and ref.²¹). The occurrence of climate-driven state transitions in ocean circulation and oxygenation is well established in the context of changes in Atlantic and Pacific basin meridional overturning since the last glacial maximum (21 ka)^{32,33}. In contrast, the potential for ocean state transitions in deeper time has received much less attention but is no less important (e.g. ref.²¹). We also have good reason to conclude that the occurrence of oscillatory ocean circulation modes is not an artifact of the particular model used here and may occur as a transitional regime between different stable steady-states (Extended Data Fig. 10). For instance, oscillations have previously been identified in both (ocean-only) 3D ocean circulation models^{34,35} and 3D ocean circulation models coupled to simplified representations of atmospheric dynamics (Earth System Models of intermediate complexity)^{36,37}. Non-steady solutions in volume-integrated ocean temperature are also hinted at in a number of recent fully coupled GCM simulations under specific continental configurations and climate

states¹⁶. Further work conducted using higher-resolution Earth system models, e.g. of the

147

148

149

150

151

152

153

154

155

156

157

158

159

160

161

162

163

164

165

166

167

168

169

170

Coupled Model Intercomparison Project phase 6 generation, will be important to distinguish robust from model-dependent modes of ocean circulation, although identifying the boundary conditions giving rise to oscillatory modes will be computationally challenging.

172

173

174

175

176

177

178

179

180

181

182

183

184

185

186

187

188

189

190

191

192

193

194

195

196

Our finding of a fundamental decoupling of subsurface and benthic [O₂] during the Phanerozoic (Fig. 1e; $R^2 = 0.001$) implies that no simple relationship exists during the Phanerozoic amongst the concentrations of oxygen in the atmosphere, the subsurface ocean, and at the seafloor. Furthermore, the highly non-linear and chaotic nature of the system means that even very minor changes in continental configuration (e.g. contrast 460 vs. 440 Ma, Figure 2) can induce dramatic re-organizations of large-scale circulation and hence ocean oxygenation, and similarly, confusticate any predictable relationship between changes in atmospheric pCO₂ (and climate) and ocean oxygenation. This has implications not only for how we interpret deep-ocean redox proxy records and specifically proxies for the global areal extent of seafloor anoxia⁵ (e.g., $\delta^{238}U^{12}$, $\delta^{98}Mo^9$), but also how we understand the underlying controls on ocean anoxia and infer changes in atmospheric composition. For instance, Stolper and Keller³⁸ analyzed the ratio of Fe^{3+} to total Fe ($Fe^{3+}/\Sigma Fe$) in hydrothermally altered basalts formed in ocean basins to quantitatively reconstruct deep-ocean [O₂] over the last 3500 Myrs. Their results suggest that the deep ocean became oxygenated only in the Phanerozoic and probably not until the late Paleozoic (<420 Myr). Our simulations support the vision of a poorly oxygenated early Paleozoic ocean^{4,5,38} (until ca. 440 Ma in the model, see Figs. 1d, 3d). However, while $Fe^{3+}/\Sigma Fe$ data is interpreted as reflecting a rise in atmospheric oxygen concentrations³⁸, our Earth System simulations in contrast suggest that deep-ocean oxygenation around 440-420 Ma could have been a consequence of continental rearrangement and concomitant changes in ocean circulation and ventilation. The implication is that early Phanerozoic atmospheric pO_2 need not have been appreciably lower than modern, which aligns with the measurements of atmospheric oxygen trapped in fluid-gas

inclusions of halite³⁹. Furthermore, the step changes in early Paleozoic seafloor oxygenation are indicative of bistability between deep-ocean circulation states; that is, for certain continental configurations multiple advection and convection patterns will co-exist (what is observed depends on the initial conditions of the simulation). Switches between such states could provide an explanation to the swings⁵ in early Paleozoic global anoxia extent documented on grounds of $\delta^{238}U^{40-42}$ and $\delta^{98}Mo^{41,43}$. Uncertainties in both the model and geological data preclude us from determining if our simulated scenario may have actually taken place in the geological past, and we recognize that continental rearrangement is also not exclusive of secular variation in other drivers of ocean anoxia, such as atmospheric oxygen, ocean nutrient inventory, and global warming^{13,19,21,26}. That said, and despite our idealized boundary conditions and invariant atmospheric chemistry, there are shared temporal trends (albeit with different timings and interval durations) with recent I/Ca-based oxygen proxy compilations¹³, namely: low oxygenation in the early and late Paleozoic with a high during the Devonian, and peak values occurring prior to late Cenozoic cooling.

Finally, our results have implications for the evolution of marine animal ecosystems through the Phanerozoic. If kyr-scale oscillations in ocean oxygenation were a characteristic feature of early Paleozoic oceans, as supported by the high-resolution Mo record of ref.⁴⁴ and our modelling (Extended Data Fig. 8), this would lend support to arguments linking the progressive (here: paleogeographical) stabilization of a steady-state Earth system to decreasing extinction rates through the Phanerozoic^{6,45}.

MAIN TEXT REFERENCES

1. Payne, J. L. *et al.* Two-phase increase in the maximum size of life over 3.5 billion years reflects biological innovation and environmental opportunity. *Proc. Natl. Acad. Sci. U. S. A.* **106**, 24–27 (2009).

- 222 2. Cole, D. B. et al. On the co-evolution of surface oxygen levels and animals.
- 223 Geobiology 18, 260–281 (2020).
- 3. Sperling, E. A., Knoll, A. H. & Girguis, P. R. The Ecological Physiology of Earth's
- Second Oxygen Revolution. Annu. Rev. Ecol. Evol. Syst. 46, 215–235 (2015).
- 4. Krause, A. J. et al. Stepwise oxygenation of the Paleozoic atmosphere. Nat. Commun.
- **9**, 4081 (2018).
- 228 5. Tostevin, R. & Mills, B. J. Reconciling proxy records and models of Earth's
- oxygenation during the Neoproterozoic and Palaeozoic. *Interface Focus* **10**, 20190137
- 230 (2020).
- Kocsis, Á. T., Reddin, C. J., Alroy, J. & Kiessling, W. The r package divDyn for
- 232 quantifying diversity dynamics using fossil sampling data. *Methods Ecol. Evol.* **10**,
- 233 735–743 (2019).
- Penn, J. L., Deutsch, C., Payne, J. L. & Sperling, E. A. Temperature-dependent
- 235 hypoxia explains biogeography and severity of end-Permian marine mass extinction.
- 236 *Science* **362**, eaat1327 (2018).
- 237 8. Edwards, C. T., Saltzman, M. R., Royer, D. L. & Fike, D. A. Oxygenation as a driver
- of the Great Ordovician Biodiversification Event. *Nat. Geosci.* **10**, 925–929 (2017).
- 239 9. Dahl, T. W., Hammarlund, E. U. & Anbar, A. D. Devonian rise in atmospheric oxygen
- correlated to the radiations of terrestrial plants and large predatory fish. *Proc. Natl.*
- 241 Acad. Sci. 107, 17911–17915 (2010).
- 242 10. Zou, C. et al. Ocean euxinia and climate change "double whammy" drove the Late
- 243 Ordovician mass extinction. *Geology* **46**, 535–538 (2018).
- 244 11. Bond, D., Wignall, P. B. & Racki, G. Extent and duration of marine anoxia during the
- Frasnian-Famennian (Late Devonian) mass extinction in Poland, Germany, Austria
- and France. Geol. Mag. 141, 173–193 (2004).

- 247 12. Lau, K. V. et al. Marine anoxia and delayed Earth system recovery after the end-
- 248 Permian extinction. *Proc. Natl. Acad. Sci.* **113**, 2360–2365 (2016).
- 249 13. Lu, W. et al. Late inception of a resiliently oxygenated upper ocean. Science 5,
- 250 eaar5372 (2018).
- 251 14. Sperling, E. A. et al. A long-term record of early to mid-Paleozoic marine redox
- 252 change. *Sci. Adv.* (2021) doi:10.1126/sciadv.abf4382.
- 253 15. Lenton, T. M. et al. Earliest land plants created modern levels of atmospheric oxygen.
- 254 Proc. Natl. Acad. Sci. U. S. A. 201604787 (2016).
- 255 16. Valdes, P., Scotese, C. & Lunt, D. Deep Ocean Temperatures through Time. Clim.
- 256 *Past* **17**, 1483–1506 (2021).
- 257 17. Farnsworth, A. et al. Climate Sensitivity on Geological Timescales Controlled by
- Nonlinear Feedbacks and Ocean Circulation. *Geophys. Res. Lett.* **6**, 19 (2019).
- 259 18. Scotese, C. R., Song, H., Mills, B. J. W. & van der Meer, D. G. Phanerozoic
- paleotemperatures: The earth's changing climate during the last 540 million years.
- 261 Earth-Science Rev. 103503 (2021) doi:10.1016/j.earscirev.2021.103503.
- 262 19. Monteiro, F. M., Pancost, R. D., Ridgwell, A. & Donnadieu, Y. Nutrients as the
- dominant control on the spread of anoxia and euxinia across the Cenomanian-Turonian
- oceanic anoxic event (OAE2): Model-data comparison. *Paleoceanography* 27, (2012).
- 265 20. Ridgwell, A. et al. Marine geochemical data assimilation in an efficient Earth system
- 266 model of global biogeochemical cycling. *Biogeosciences* **4**, 87–104 (2007).
- 267 21. Pohl, A. et al. Vertical decoupling in Late Ordovician anoxia due to reorganization of
- ocean circulation. Nat. Geosci. 14, (2021).
- 269 22. Ward, B. A. et al. EcoGEnIE 0.1: plankton ecology in the cGENIE Earth system
- 270 model. Geosci. Model Dev. 11, 4241–5267 (2018).
- 271 23. Crichton, K. A., Wilson, J. D., Ridgwell, A. & Pearson, P. N. Calibration of key

- temperature-dependent ocean microbial processes in the cGENIE. muffin Earth system
- 273 model. Geophys. Model Dev. Discuss. (2020).
- 274 24. Scotese, C. R. & Wright, N. PALEOMAP Paleodigital Elevation Models
- 275 (PaleoDEMS) for the Phanerozoic (PALEOMAP Project, 2018).
- 276 https://www.earthbyte.org/paleodem-resource- scotese-and-wright-2018/ (2018).
- 277 25. Pohl, A. et al. Quantifying the paleogeographic driver of Cretaceous carbonate
- 278 platform development using paleoecological niche modeling. *Palaeogeogr.*
- 279 *Palaeoclimatol. Palaeoecol.* **514**, 222–232 (2019).
- 280 26. Hülse, D. et al. End-Permian marine extinction due to temperature-driven nutrient
- recycling and euxinia. *Nat. Geosci.* **14**, (2021).
- 282 27. Baudin, F. & Riquier, L. The late hauterivian faraoni 'oceanic anoxic event': An
- 283 update. Bull. la Soc. Geol. Fr. 185, 359–377 (2014).
- 284 28. Laugié, M. et al. Exploring the impact of Cenomanian paleogeography and marine
- gateways on oceanic oxygen. *Paleoceanogr. Paleoclimatology* **36**, e2020PA004202
- 286 (2021).
- 287 29. De Vleeschouwer, D. et al. Timing and pacing of the Late Devonian mass extinction
- event regulated by eccentricity and obliquity. *Nat. Commun.* **8**, 2268 (2017).
- 289 30. Ruvalcaba Baroni, I. et al. Ocean Circulation in the Toarcian (Early Jurassic): A Key
- 290 Control on Deoxygenation and Carbon Burial on the European Shelf. *Paleoceanogr.*
- 291 *Paleoclimatology* **33**, 994–1012 (2018).
- 292 31. Torsvik, T. H. BugPlates: Linking Biogeography and Palaeogeography Software
- 293 Installation. (2009).
- 294 32. Ferreira, D., Marshall, J., Ito, T. & McGee, D. Linking Glacial-Interglacial States to
- Multiple Equilibria of Climate. *Geophys. Res. Lett.* **45**, 9160–9170 (2018).
- 296 33. Jaccard, S. L. & Galbraith, E. D. Large climate-driven changes of oceanic oxygen

- concentrations during the last deglaciation. *Nat. Geosci.* **5**, 151–156 (2012).
- 298 34. Weijer, W. & Dijkstra, H. A. Multiple oscillatory modes of the global ocean
- 299 circulation. J. Phys. Oceanogr. **33**, 2197–2213 (2003).
- 300 35. Sirkes, Z. & Tziperman, E. Identifying a damped oscillatory thermohaline mode in a
- general circulation model using an adjoint model. J. Phys. Oceanogr. 31, 2297–2306
- 302 (2001).
- 303 36. Meissner, K. J., Eby, M., Weaver, A. J. & Saenko, O. A. CO2 threshold for millennial-
- scale oscillations in the climate system: Implications for global warming scenarios.
- 305 *Clim. Dyn.* **30**, 161–174 (2008).
- 306 37. Haarsma, R. J., Opsteegh, J. D., Selten, F. M. & Wang, X. Rapid transitions and ultra-
- low frequency behaviour in a 40 kyr integration with a coupled climate model of
- 308 intermediate complexity. *Clim. Dyn.* **17**, 559–570 (2001).
- 309 38. Stolper, D. A. & Keller, C. B. A record of deep-ocean dissolved O2 from the oxidation
- state of iron in submarine basalts. *Nature* **553**, 323–327 (2018).
- 311 39. Brand, U. et al. Atmospheric oxygen of the Paleozoic. Earth-Science Rev. 216, (2021).
- 312 40. Dahl, T. W. et al. Reorganisation of earth's biogeochemical cycles briefly oxygenated
- 313 the oceans 520 myr ago. *Geochemical Perspect. Lett.* **10**, 210–220 (2019).
- 314 41. Wei, G. Y. et al. Global marine redox evolution from the late Neoproterozoic to the
- early Paleozoic constrained by the integration of Mo and U isotope records. *Earth*-
- 316 Science Rev. **214**, 103506 (2021).
- 317 42. Wei, G. Y. et al. Marine redox fluctuation as a potential trigger for the Cambrian
- 318 explosion. *Geology* **46**, 587–590 (2018).
- 319 43. Kendall, B. et al. Uranium and molybdenum isotope evidence for an episode of
- widespread ocean oxygenation during the late ediacaran period. *Geochim. Cosmochim.*
- 321 *Acta* **156**, 173–193 (2015).

- 322 44. Dahl, T. W. et al. Brief oxygenation events in locally anoxic oceans during the
- 323 Cambrian solves the animal breathing paradox. Sci. Rep. 9, 1–9 (2019).
- 324 45. Payne, J. L., Bachan, A., Heim, N. A., Hull, P. M. & Knope, M. L. The evolution of
- 325 complex life and the stabilization of the Earth system: Complex life and the Earth
- 326 system. *Interface Focus* **10**, (2020).
- 327 46. Cao, L. et al. The role of ocean transport in the uptake of anthropogenic CO2.
- 328 *Biogeosciences* **6**, 375–390 (2009).

METHODS

330

331

332

333

334

335

336

337

338

339

340

341

342

343

344

345

346

347

348

349

350

351

352

353

354

Description of the model

dimensional ocean circulation model which, for speed, is coupled to a 2D energy-moisturebalance atmospheric component. We configured the model on a 36×36 equal-area grid with 16 unevenly spaced vertical levels to a maximum 5500 m depth in the ocean. The cycling of carbon and associated tracers in the ocean is based on a single (phosphate) nutrient limitation of biological productivity accounting for plankton ecology based on Ward et al.²² and Wilson et al.⁴⁷, but adopts the Arrhenius-type temperature-dependent scheme for the remineralization of organic matter exported to the ocean interior of Crichton et al.²³. We further modify the ecological model of Ward et al.²² to account for limitation of productivity under sea ice, rescale the global mean annual C/P ratio of exported particulate organic matter to match that of the standard model (106)⁴⁶, and only diagnose the ocean surface mixed layer depth for calculating light attenuation rather than entrain this into the physical circulation. We include a sulphate (SO₄²-) tracer as an electron acceptor in the model in addition to dissolved oxygen, such that when O₂ starts to approach zero, sulphate reduction occurs in association with the remineralization of organic matter. The hydrogen sulphide (H₂S) thereby created is transported via ocean circulation and oxidized in the presence of O₂ to re-form sulphate. Note that we do not include a nitrogen cycle (and hence nitrate reduction), nor methanogenesis in our model tracer configuration. See ref. 48 and ref. 49 for details of the overall ocean redox scheme. Despite its low spatial resolution, cGENIE satisfactorily simulates first-order ocean [O₂] spatial patterns and values for the present-day ocean when configured with pre-industrial boundary conditions such as 278 ppm CO₂ (Extended Data Fig. 1 and ref.²⁰), as well as in the geological past^{19,21}. For instance, simulations for Oceanic Anoxic Event 2 conducted using

cGENIE²⁰ – an 'Earth System Model of intermediate complexity' – is based around a 3-

cGENIE (ref. 19, their Fig. 2f,g) compare well with simulations conducted using the more complex model IPSL-CM5A2 (ref.²⁸, their Fig. 10), in terms of both global extent of anoxia and response to gateway alteration. **Description of the numerical experiments** We adopted the (flat-bottomed) Phanerozoic continental reconstructions of Scotese and Wright²⁴, but substituted the deep-ocean bathymetry of Müller et al.⁵⁰ when available (140 Ma - 0 Ma) in order to account for mid-ocean ridges. In order to specifically quantify the impact of paleogeographical evolution, we kept solar luminosity (1368 W m⁻²), atmospheric oxygen concentrations (20.95 %), and ocean nutrient inventory (2.1 µmol kg⁻¹ PO₄), invariant. We employed a null eccentricity-minimum obliquity orbital configuration, which provides an equal mean annual insolation to both hemispheres with minimum seasonal contrasts. Atmospheric CO₂ concentration was kept fixed in series #1 (2240 ppm) but varied in series #2 in order to approximately 'correct' for the paleogeographical impacts on climate. These forcing combinations ensured that simulated ocean temperatures are in the right order of magnitude compared with the Phanerozoic proxy-derived trend¹⁸. The mean Phanerozoic tropical (25°S–25°N) sea-surface temperature is 29.67°C (standard deviation: 1.88°C) in series #1 (mean of 29.39°C and standard deviation of 0.45°C in series #2) compared to a mean of 28.1°C (standard deviation: 2.51°C) in the data compilation¹⁸. To generate the physical atmospheric boundary conditions required by cGENIE for each different continental configuration, we ran FOAM⁵¹ general circulation model experiments for 2 to 3 kyrs, until deep-ocean temperature equilibrium. We then derived the 2D wind speed and wind stress, and 1D zonally-averaged albedo forcing fields required by the cGENIE model, using the 'muffingen' open-source software (DOI:

10.5281/zenodo.5500687), following the methods employed in ref⁵². Importantly, the FOAM

355

356

357

358

359

360

361

362

363

364

365

366

367

368

369

370

371

372

373

374

375

376

377

ocean-atmosphere simulations (and derived cGENIE forcing fields) account for topography on land, after ref.²⁴ (although topography is not shown in our maps for readability).

Simulations were initialized with a sea-ice free ocean and homogeneous temperature and salinity in the ocean (5 °C and 33.9 ‰, respectively) and integrated for a total of 20,000 years. Data is presented reflecting either the average over the last 5,000 years of the simulation (e.g., Fig. 2), or the mean and range of any oscillation over the last 5,000 years (e.g., Figs 1, 3), as detailed in the figure captions.

Principal component analysis

Principal components analyses (PCA) of Fig. 1 and Extended Data Fig. 5 were performed using, for each variable, the mean value simulated over the last 5000 years of the model simulations. For each variable, a total of 28 values was thus obtained (one value for each of the 28 time slices, from 540 Ma to 0 Ma every 20 Myrs). We considered 13 variables: surface [O2], subsurface [O2], benthic [O2], global [O2], global water age, benthic water age, seasurface temperature ('SST'), benthic temperature, pCO2, meridional overturning circulation maximum ('MOC max') and minimum ('MOC min'), export production ('export'; i.e., the flux of organic carbon produced in the ocean photic zone by primary producers that is not recycled (remineralised) before sinking deeper in the water column) and total ocean area. The PCA was conducted using the 'PCA' function of the R package 'FactoMineR' and the first two axes / principal components were represented (capturing ca. 68 % of the variance in both cases). The objective here is not to provide a thorough PCA analysis but rather to (1) confirm the robustness of the correlations illustrated in the form of time-series and R² in the other panels of Fig. 1 and Extended Data Fig. 5 and (2) provide information on the correlation (or not) of additional key variables in a synthetic and graphical manner.

Additional discussion on ocean circulation regimes

Most of the simulations in Extended Data Figs. 8a and 8b show that ocean dynamics obtain

stable steady-state solutions. However, amongst these are cases where the system overshoots (for example, compare 0 Ma and 120 Ma in Extended Data Fig. 8a) before approaching a steady-state solution. This may imply the presence of an unstable oscillatory mode, in agreement with the linear stability analysis of low-resolution GCM steady states under present-day conditions^{34,35}. The simulations in Extended Data Fig. 8 reveal that, depending on changes to continental configuration, the steady-state solutions can lose stability, resulting in stable oscillations. It is known that, under certain climate conditions, advective feedbacks in the ocean circulation can destabilize the steady state⁵⁴. Simulations for 540 Ma and 500 Ma in Extended Data Figs. 8a and 8b, respectively, are cases of steady-state solutions with oscillatory modes that are linearly stable, but only weakly stable, resulting in clear examples of damped oscillations. Since the frequencies of the damped and self-sustained oscillations (500 and 520 Ma in Extended Data Fig. 8b, respectively) are very similar, the transition could represent a Hopf bifurcation, resulting in self-sustained oscillations (characterized by fluctuations in circulation pattern and strength) around an unstable steady state. In order to better understand the model behavior and ultimately, the nature of the state transitions in the global ocean circulation, we conducted additional cGENIE simulations using two contrasting, idealized continental configurations featuring either a latitudinal strip of land from the North Pole to the Southern Hemisphere mid latitudes ('Drake world'55), or a strip of land extending from the North Pole to the South Pole ('ridge world'55) (Extended Data Fig. 10). Drake world, with a pole free of land (i.e., purely oceanic at all longitudes), schematically represents the continental configuration of the early Paleozoic (or a high latitude circumpolar path such as in the late Cenozoic), while ridge world represents an early Mesozoic-like continental arrangement with landmasses present from the North Pole to the

404

405

406

407

408

409

410

411

412

413

414

415

416

417

418

419

420

421

422

423

424

425

426

427

428

South Pole (see Fig. 2).

With Drake world, at low pCO₂ levels, deep-water formation takes place at the North

Pole, where a slightly higher hemispherical fraction of land cover with lower thermal inertia favors winter cooling over the surrounding ocean and thus convection (label #1 in Extended Data Figs. 10a and 10b). As atmospheric CO₂ is steadily increased across a series of experiments, the onset of a first set of oscillations, between ×5.5 and ×7.5 CO₂ (label #2), marks the appearance of a new mode of ocean circulation that stabilizes in the subsequent stable steady state at around ×8.25 CO₂ (label #3). Then, a new set of oscillations, from ×9 to ×9.75 CO₂, marks another step toward the weakening of the deep-water formation over the North Pole and strengthening over the South Pole (label #4). A third stable equilibrium finally stabilizes above ×10.75 CO₂ (label #5). Each set of oscillations thus marks the shift to a new regime of steady-state circulation and the ultimate result is a shift in the locus of deepwater formation from the North Pole (with lands barriers) to the South Pole (oceanic) in response to global warming from ×4 to ×16 CO₂. A comparable (but latitudinally reversed) behavior was previously observed by Pohl et al.²¹ for the latest Ordovician. In response to global warming (their Figs. 4e to 4i, see also Extended Data Fig. 10c), the locus of deepwater formation shifts in their simulations from the South Pole (with lands) to the North Pole (oceanic). This is very similar to the change in ocean circulation simulated between 460 Ma and 440 Ma in simulation series #1 (Fig. 2), although the state transition here involves continental rearrangement in addition to global warming (global sea-surface temperature increases from 24.1°C at 460 Ma to 24.38°C at 440 Ma). No similar state transition is observed using the ridge world configuration (Extended Data Fig. 10a).

449

450

429

430

431

432

433

434

435

436

437

438

439

440

441

442

443

444

445

446

447

448

METHODS REFERENCES

Wilson, J. D., Monteiro, F. M., Schmidt, D. N., Ward, B. A. & Ridgwell, A. Linking
Marine Plankton Ecosystems and Climate: A New Modeling Approach to the Warm
Early Eocene Climate. *Paleoceanogr. Paleoclimatology* 33, 1439–1452 (2018).

- 454 48. T. Reinhard, C. et al. Oceanic and atmospheric methane cycling in the cGENIE Earth
- 455 system model Release v0.9.14. *Geosci. Model Dev.* **13**, 5687–5706 (2020).
- 456 49. Velde, S. J. Van De, Hülse, D., Reinhard, C. T. & Ridgwell, A. Iron and sulfur cycling
- in the cGENIE. muffin Earth system model (v0.9.21). Geosci. Model Dev. 14, 2713–
- 458 2745 (2021).
- 459 50. Müller, R. D., Sdrolias, M., Gaina, C., Steinberger, B. & Heine, C. Long-term sea-
- level fluctuations driven by ocean basin dynamics. *Science* **319**, 1357–1362 (2008).
- 461 51. Jacob, R. L. Low frequency variability in a simulated atmosphere-ocean system.
- 462 (University of Wisconsin Madison, 1997).
- 463 52. Crichton, K., Ridgwell, A., Lunt, D., Farnsworth, A. & Pearson, P. Data-constrained
- assessment of ocean circulation changes since the middle Miocene in an Earth system
- 465 model. Clim. Past Discuss. 1–36 (2020) doi:10.5194/cp-2019-151.
- 466 53. Lê, S., Josse, J. & Husson, F. FactoMineR: An R package for multivariate analysis. J.
- 467 *Stat. Softw.* **25**, 1–18 (2008).
- 468 54. Weijer, W. et al. Stability of the Atlantic Meridional Overturning Circulation: A
- 469 Review and Synthesis. J. Geophys. Res. Ocean. 124, 5336–5375 (2019).
- 470 55. Ferreira, D., Marshall, J. & Campin, J. M. Localization of deep water formation: Role
- of atmospheric moisture transport and geometrical constraints on ocean circulation. J.
- 472 *Clim.* **23**, 1456–1476 (2010).
- 473 56. Garcia, H. et al. World Ocean Atlas 2018, Volume 3: Dissolved Oxygen, Apparent
- 474 Oxygen Utilization, and Dissolved Oxygen Saturation. (2019).
- 475 57. Marsh, R. et al. Bistability of the thermohaline circulation identified through
- comprehensive 2-parameter sweeps of an efficient climate model. Clim. Dyn. 23, 761–
- 477 777 (2004).
- 478 58. DeVries, T. & Holzer, M. Radiocarbon and Helium Isotope Constraints on Deep

- Ocean Ventilation and Mantle-3He Sources. *J. Geophys. Res. Ocean.* **124**, 3036–3057
- 480 (2019).
- 481 59. Song, H. et al. The onset of widespread marine red beds and the evolution of
- ferruginous oceans. *Nat. Commun.* **8**, (2017).
- 483 60. Melchin, M. J., Mitchell, C. E., Holmden, C. & Štorch, P. Environmental changes in
- 484 the Late Ordovician-early Silurian: Review and new insights from black shales and
- 485 nitrogen isotopes. *Geol. Soc. Am. Bull.* **125**, 1635–1670 (2013).
- 486 61. Pohl, A., Nardin, E., Vandenbroucke, T. R. A. & Donnadieu, Y. High dependence of
- Ordovician ocean surface circulation on atmospheric CO2 levels. *Palaeogeogr.*
- 488 *Palaeoclimatol. Palaeoecol.* **458**, 39–51 (2016).
- 489 62. Meyer, K. M., Ridgwell, A. & Payne, J. L. The influence of the biological pump on
- ocean chemistry: implications for long-term trends in marine redox chemistry, the
- 491 global carbon cycle, and marine animal ecosystems. *Geobiology* **14**, 207–219 (2016).

- 493 **CODE AVAILABILITY**
- The version of the cGENIE code used in this paper is tagged as release v0.9.29 and has a
- 495 DOI: 10.5281/zenodo.5885685. Necessary boundary condition files are included as part of
- 496 the code release. Configuration files for the specific experiments presented in the paper can
- be found in the installation subdirectory: genie-
- 498 userconfigs/MS/pohletal.Nature.2022. Details of the experiments, plus the command
- line needed to run each one, are given in the readme.txt file in that directory. A manual
- describing code installation, basic model configuration, and an extensive series of tutorials is
- provided (DOI: 10.5281/zenodo.5500696). The FOAM output is hosted on Zenodo (DOI:
- 502 10.5281/zenodo.5780096).

503 **ACKNOWLEDGMENTS**

504	The authors thank 4 anonymous reviewers for their comments, and J. Mossinger for editorial
505	handling. This project has received funding from the European Union's Horizon 2020 research
506	and innovation programme under the Marie Sklodowska-Curie grant agreement No. 838373.
507	Calculations were partly performed using HPC resources from DNUM CCUB (Centre de
508	Calcul de l'Université de Bourgogne). A.R. acknowledges support from NSF grants 1736771
509	and EAR-2121165, as well as from the Heising-Simons Foundation. This is a contribution to
510	UNESCO project IGCP 735 "Rocks and the Rise of Ordovician Life" (Rocks n' ROL).
511	AUTHOR CONTRIBUTIONS
512	A.P. and A.R. designed the study and wrote the manuscript with input from all co-authors.
513	AP. and A.R. conducted the FOAM and cGENIE experiments. A.P., A.R. and A.K. led the
514	analysis of the model results. C.R.S. produced the continental reconstructions.
515	COMPETING INTERESTS
516	The authors declare no competing interests.
517	ADDITIONAL INFORMATION
518	Correspondence and requests for materials should be addressed to A.P. and A.R.
519	Peer review information.
520	Reprints and permissions information is available at www.nature.com/reprints .
521	

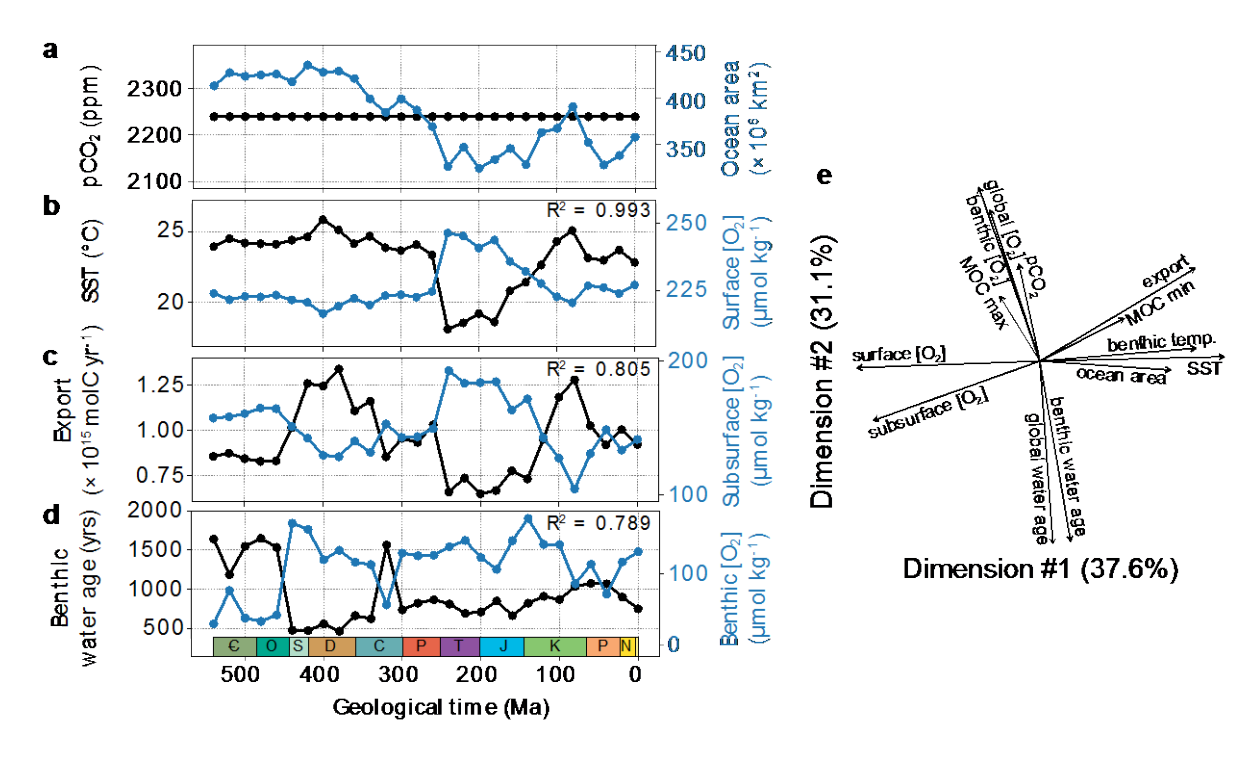


Figure 1. Earth System Model results for simulations at 2240 ppm CO₂ (series #1). (a) Atmospheric pCO₂ and global ocean area. (b) Globally averaged sea-surface temperatures and globally averaged ocean-surface oxygen concentrations. (c) Total export production and globally averaged subsurface (ca. 90–190 m depth) oxygen concentrations. (d) Globally averaged benthic water age and benthic oxygen concentrations, both extracted below 1000 m depth. For comparison, the present-day value is ~1050 years in the standard Modern cGENIE simulations of ref.⁴⁶. (e) Principal component analysis (Methods). In panels b–d, the linear correlation coefficient (R²) value is provided in the upper-right corner. For each variable and age, the mean value simulated over the last 5000 years of the model run is shown (point), while envelopes (grey shading) represent the range of values simulated over the same time interval (for simulations exhibiting oscillations). MOC: meridional overturning circulation.

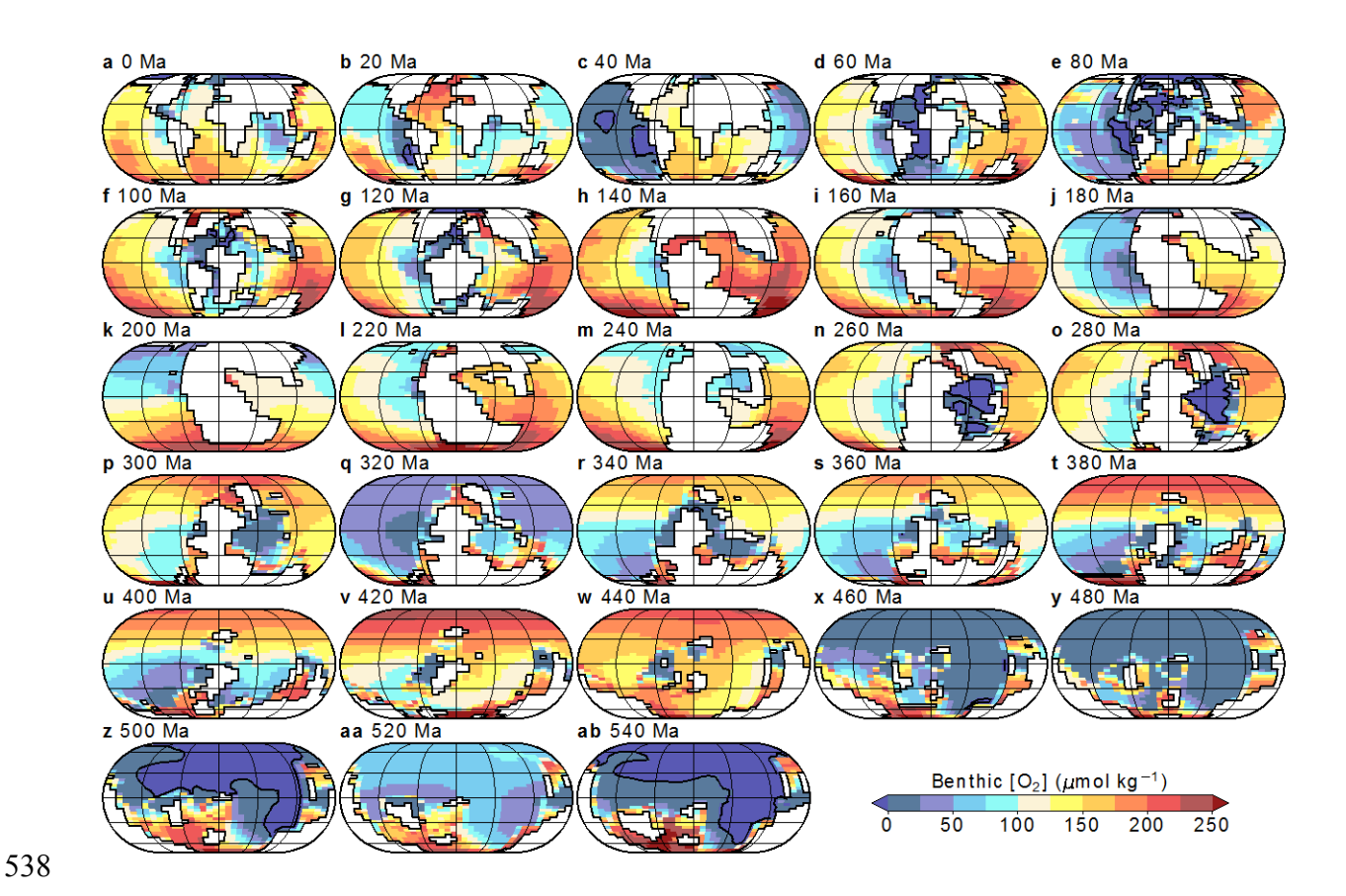


Figure 2. Benthic oxygen concentrations for simulations at 2240 ppm CO₂ (series #1). Eckert IV projection. Emerged continental masses are shaded white. Thick black line delimits the extent of oceanic anoxia, defined as $[O_2] \le 0$ µmol kg⁻¹. Results are averaged over the last 5000 years. See Extended Data Fig. 2 for magnified versions of 7 panels with redox proxy data points and Extended Data Fig. 3 for the meridional overturning circulation and regions of deep-water formation.



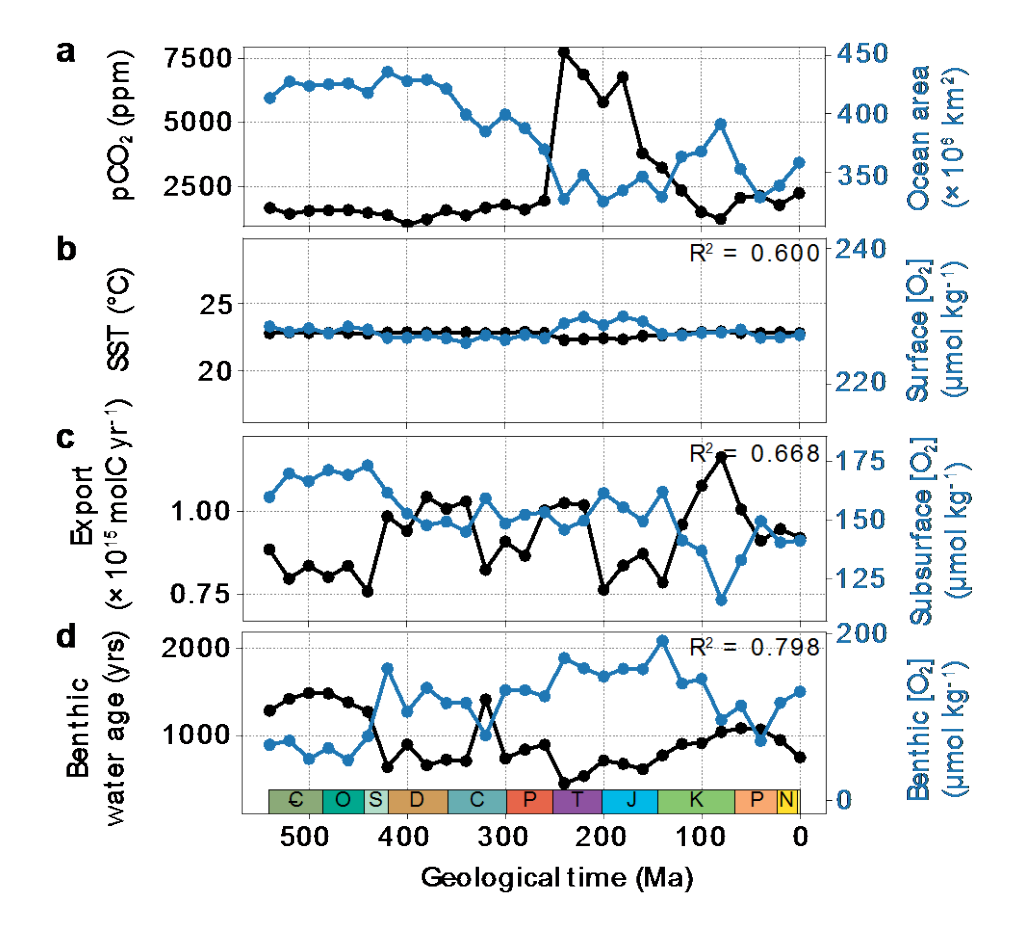
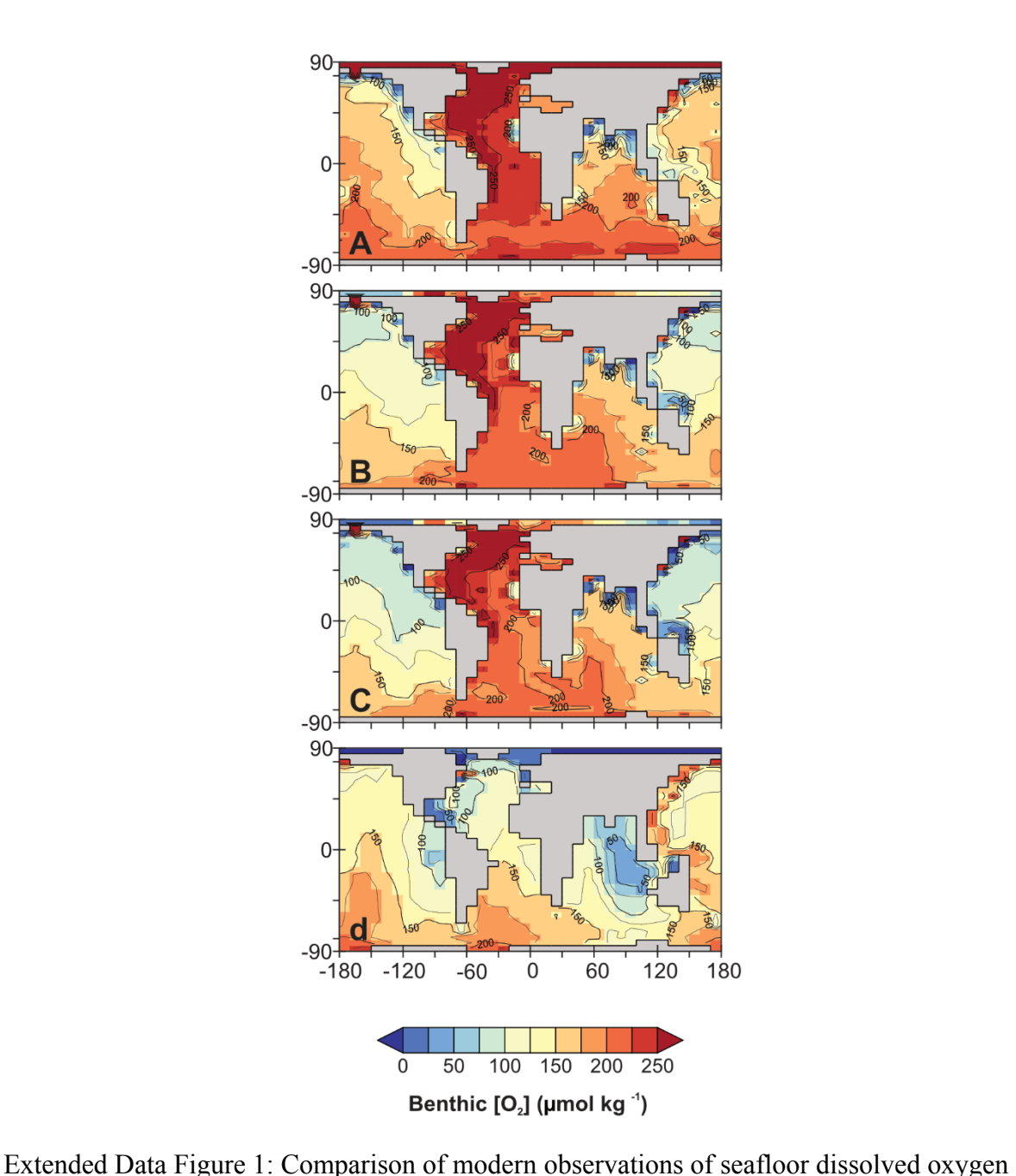


Figure 3. Panels (a-d) and panel description as per for Fig. 1, but for Earth System Model experiments in which we varied pCO_2 in order to approximately 'correct' for the paleogeographical impacts on climate (series #2), leaving surface oxygenation and mean global SST (b) largely invariant.



([O₂]) with the cGENIE model for different (modern) continental grids, boundary conditions, and biogeochemical cycling parameterization assumption. Projection is equal-area rectangular, and the color-scale is chosen to approximately match that in Figure 2. (a) Present-day distribution of [O₂] globally at the seafloor, for which we re-grid the World Ocean Atlas 2018⁵⁶ data to the modern continental grid of ref.⁴⁶ and show the oxygen concentration in the deepest model grid point. Apparent is both the production and southwards propagation (via North Atlantic Deep Water (NADW)) of highly oxygenated

waters from the North Atlantic, and oxygenated deep-water production and mixing around Antarctica. (b) Benthic [O₂] distribution for the 'standard' modern ocean circulation of ref. ⁴⁶ run at 278 ppm CO₂, plus simplified biological export scheme. The large-scale patterns of benthic [O₂] are reasonably reproduced, with the exception of too weak mixing of oxygen around the Southern Ocean, itself caused by a weak simulated Antarctic Circumpolar Current (ACC) and the difficulty in adequately representing the Drake Passage at this resolution. The slightly too-low compared to observations values in the North Pacific are an additional consequence of this. (c) Test of substituting the simplified biological export scheme of ref. 46 with the explicit ecosystem model used here in the Phanerozoic series of simulations (but still at 278 ppm CO₂). The slightly greater export simulated by the ecological model reduces benthic [O₂] by ca. 10-20 umol kg⁻¹ while leaving the large-scale patterns largely unaltered. (d) Deep-sea oxygenation in the 0 Ma Phanerozoic simulation (as per Figure 2, panel a) run at 2240 ppm CO₂. Without flux adjustment applied in the simplified cGENIE 2D EMBM atmosphere (see ref. 57) there is virtually no NADW, explaining the relatively poor and Southto-North oxygenation of the Atlantic. The Indian Ocean is also too poorly oxygenated, although the general pattern in the Pacific is reproduced. There are several main reasons for this model-data mismatch. Firstly, directly re-gridding from a relatively coarse resolution GCM (FOAM) creates a highly restricted and shallow Drake Passage (Extended Data Figure 7a, 0 Ma), precluding a strong ACC forming. More pertinently, the Phanerozoic simulation series (Figure 2) are all run at 2240 ppm. The resulting much-warmer-than-modern ocean is associated with the absence of any sea-ice formation and lower seawater oxygen solubility. likely explaining at least some of the spatial pattern and much of the lower global mean [O₂] inventory (Extended Data Figure 8a, 0 Ma). In terms of ventilation and water mass idealized mean age (not shown), the Atlantic, lacking an AMOC is far too old, whereas the Indian and

563

564

565

566

567

568

569

570

571

572

573

574

575

576

577

578

579

580

581

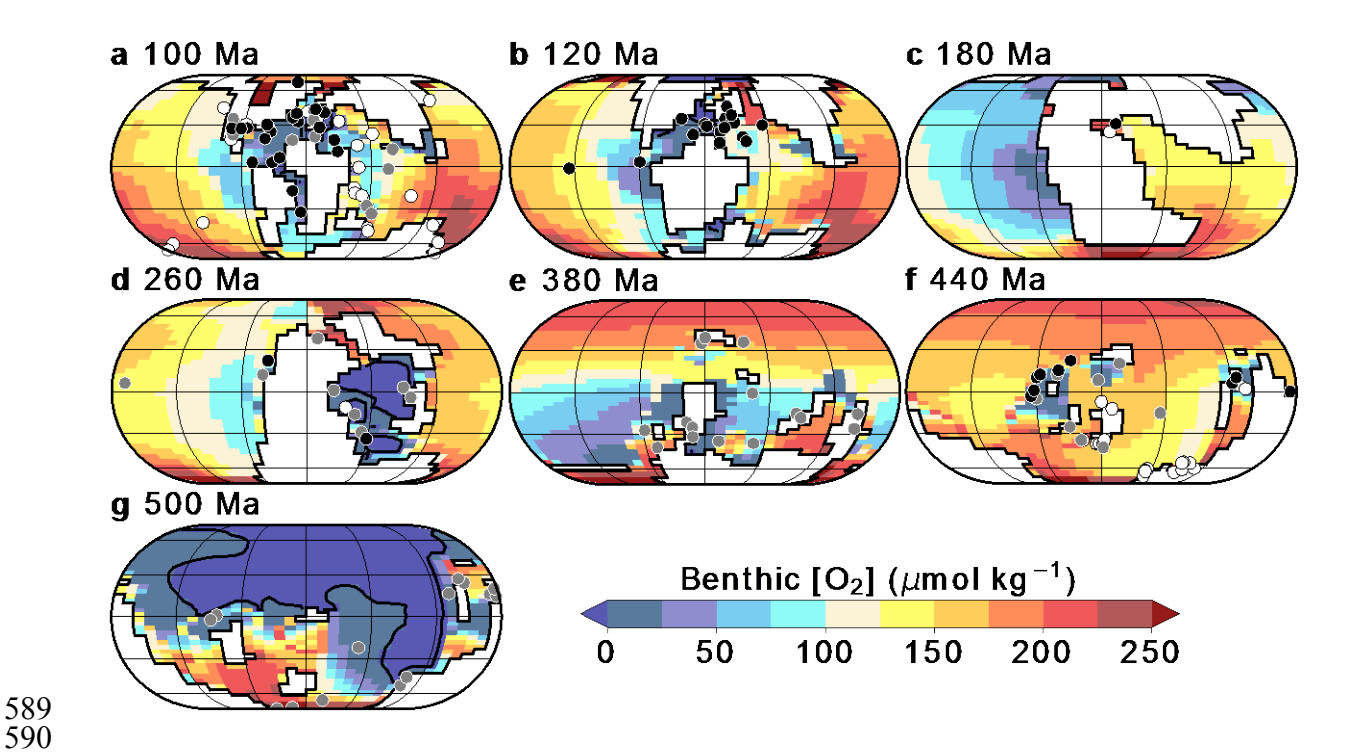
582

583

584

585

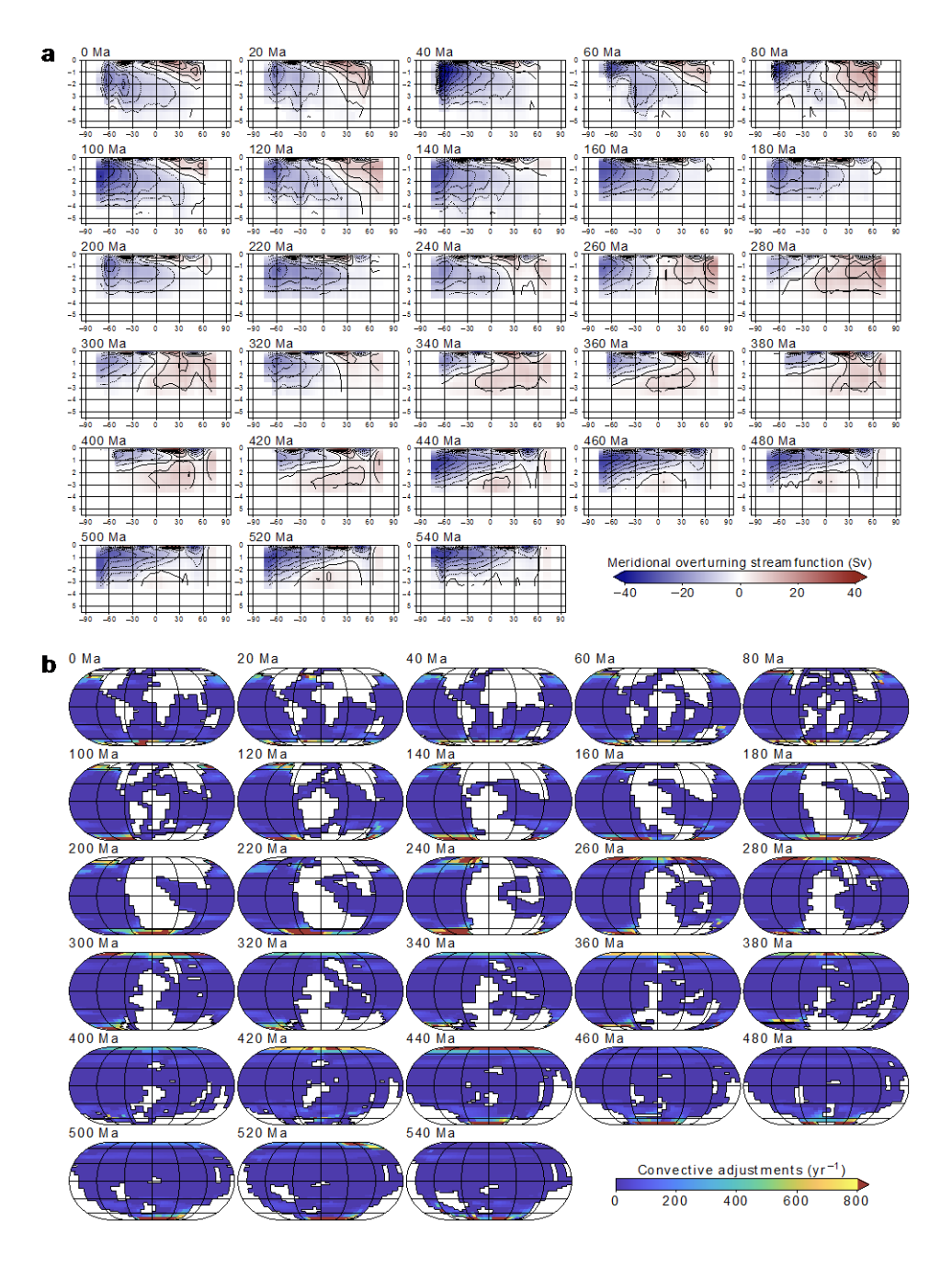
- Pacific oceans are similar to the inverse modelling of ref.⁵⁸ despite the aforementioned issues
- with the Drake Passage and that the 0 Ma simulation is run at 2240 ppm CO₂.



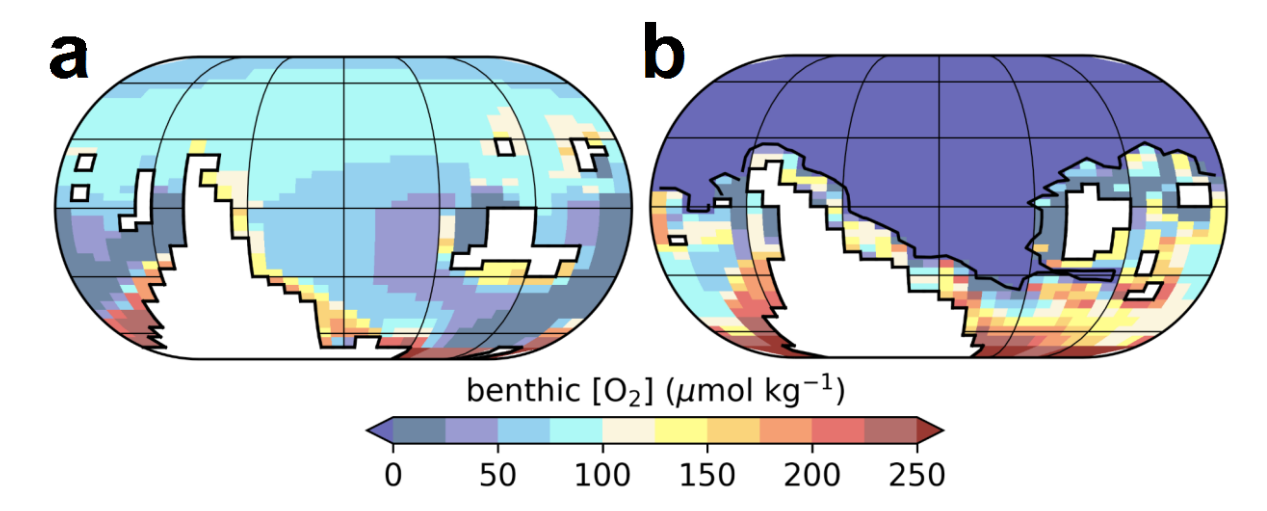
Extended Data Figure 2: Selected redox proxy data vs. the corresponding model oxygenation realization. Benthic oxygen concentrations for simulations at 2240 ppm CO₂ (series #1). Eckert IV projection. Emerged continental masses are shaded white. Thick black line delimits the extent of oceanic anoxia, defined as $[O_2] \le 0$ µmol kg⁻¹. Results are averaged over the last 5000 years. Black (white) dots represent anoxic (oxic) conditions and grey points represent possible or intermittent anoxia, for 100 Ma after ref.²⁸, for 120 Ma after ref.²⁷, for 180 Ma after ref.³⁰, for 260 Ma after ref.²⁶, for 380 and 500 Ma after ref.⁵⁹, and for 440 Ma after ref.⁶⁰. These time slices have been chosen to represent regularly-spaced periods during the Phanerozoic, typified by oceanic anoxic events. The last 100 Myrs are deliberately left aside because (i) the ocean is overall well oxygenated during this time interval and (ii) our constant boundary conditions (deliberately chosen to isolate the role of tectonics from climate, see main text) do not (and indeed, do not intent to) reproduce the pronounced cooling trend

through the Cenozoic (especially from Early Eocene Climate Optimum (ca. 50 Ma)

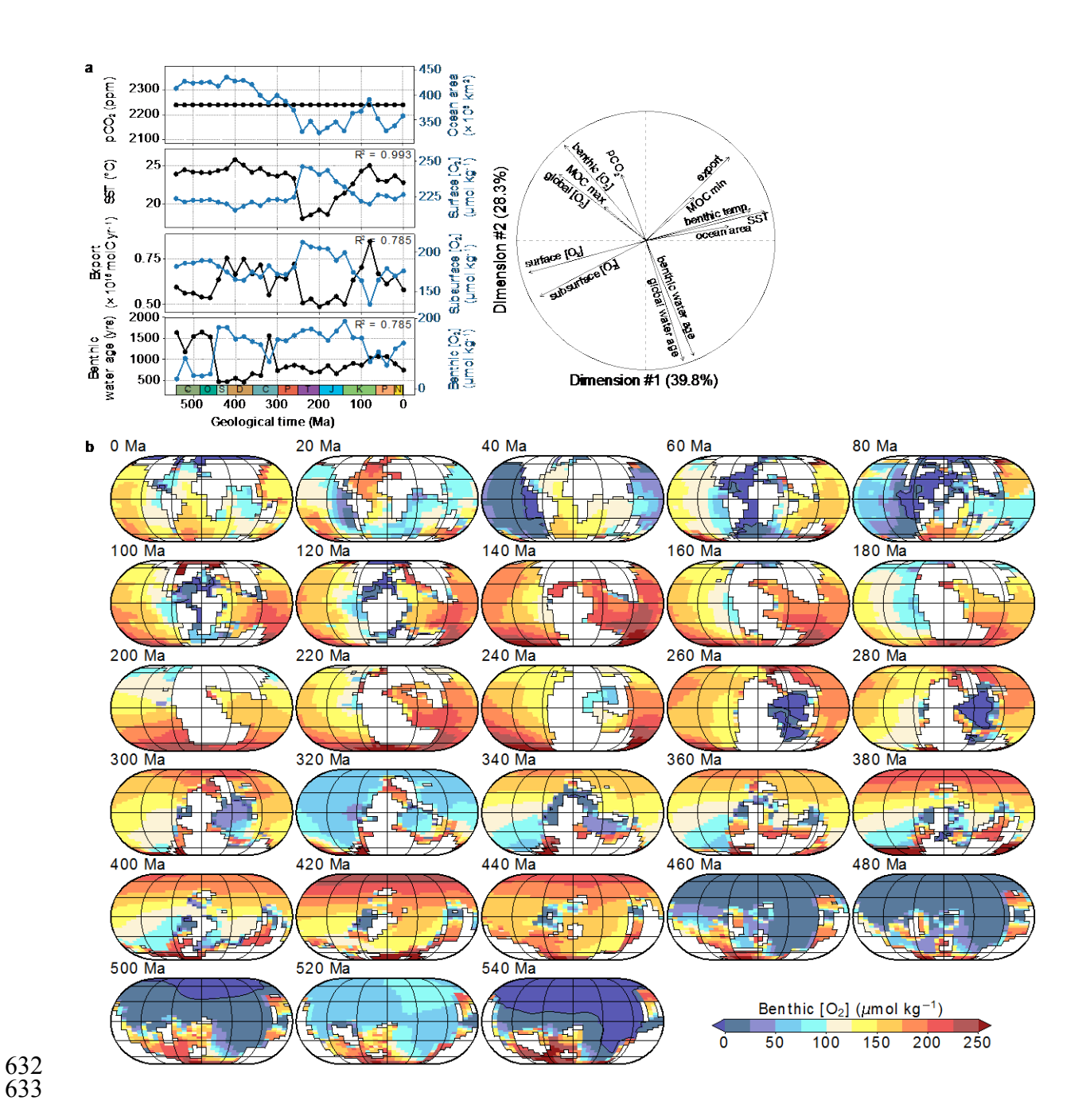
onwards), precluding direct model-data comparison.



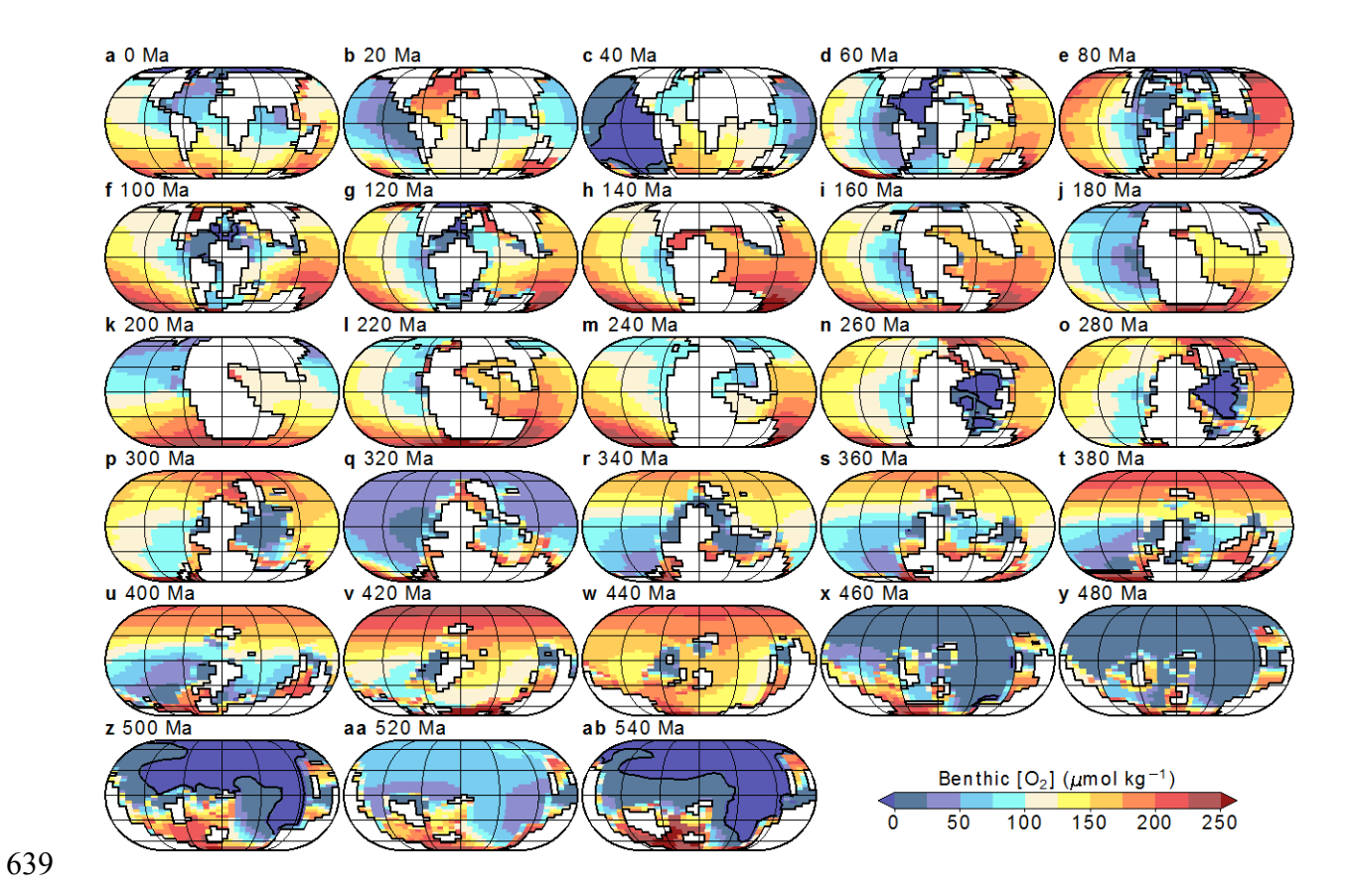
Extended Data Figure 3: Deep-ocean circulation for simulations at 2240 ppm CO_2 (series #1). (a) Meridional overturning stream function, in Sv (sverdrup, 1 Sv = 10^6 m³ s⁻¹). A negative (blue) stream function corresponds to an anticlockwise circulation. (b) Annual distribution of convective adjustments across the water column. Emerged continental masses are shaded white. Eckert IV projection. Results are averaged over the last 5000 years.



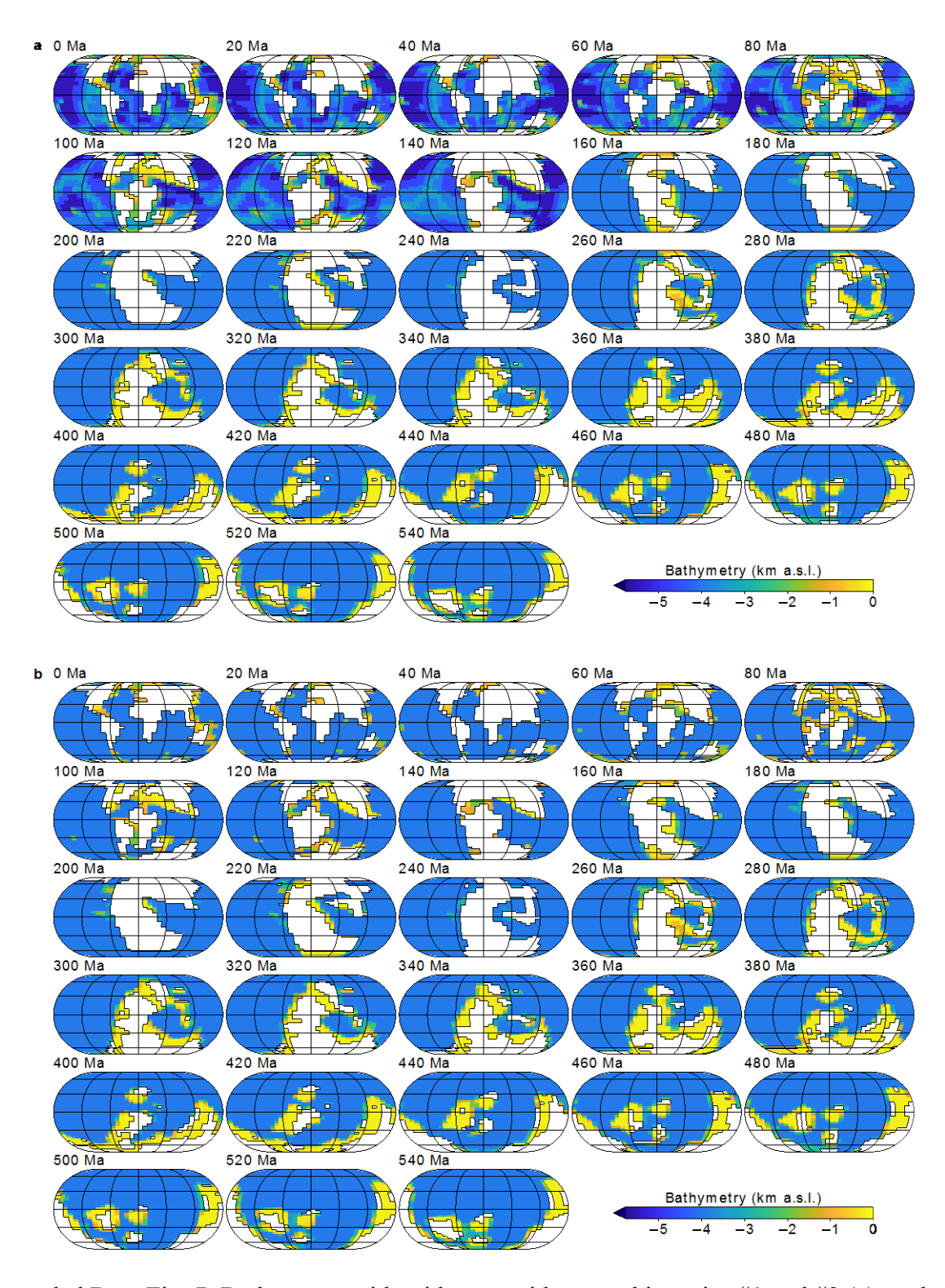
Extended Data Figure 4: Benthic oxygen concentrations for simulations at 2240 ppm CO₂ (like series #1) at 440 Ma (a) and 460 Ma (b), using the continental reconstructions of BugPlates³¹, with topography/bathymetry after ref.⁶¹. Eckert IV projection. Emerged continental masses are shaded white. Thick black line delimits the extent of oceanic anoxia, defined as $[O_2] \le 0 \mu \text{mol kg}^{-1}$. Results are averaged over the last 5000 years. Panels (a) and (b) are identical to panels (w) and (x) of Fig. 2 except that simulations have been conducted using another continental reconstruction. Note that although we simulate sulphate reduction in cGENIE, with SO_4^{2-} being used as the electron acceptor for the remineralization of organic matter in the ocean interior once dissolved O_2 has become depleted (see ref.⁴⁸), small negative O_2 concentrations can arise when multiple geochemical reactions compete simultaneously for the same depleted oxygen pool. However, because the product of sulphate reduction – hydrogen sulphide (H_2S) – has fast oxidation kinetics in the presence of free oxygen, the transport of H_2S from anoxic to oxic areas closely mirrors the transport and fate of 'negative oxygen' (see ref.⁶²) and the overall redox landscape is largely independent of this small modelled oxygen over-consumption.



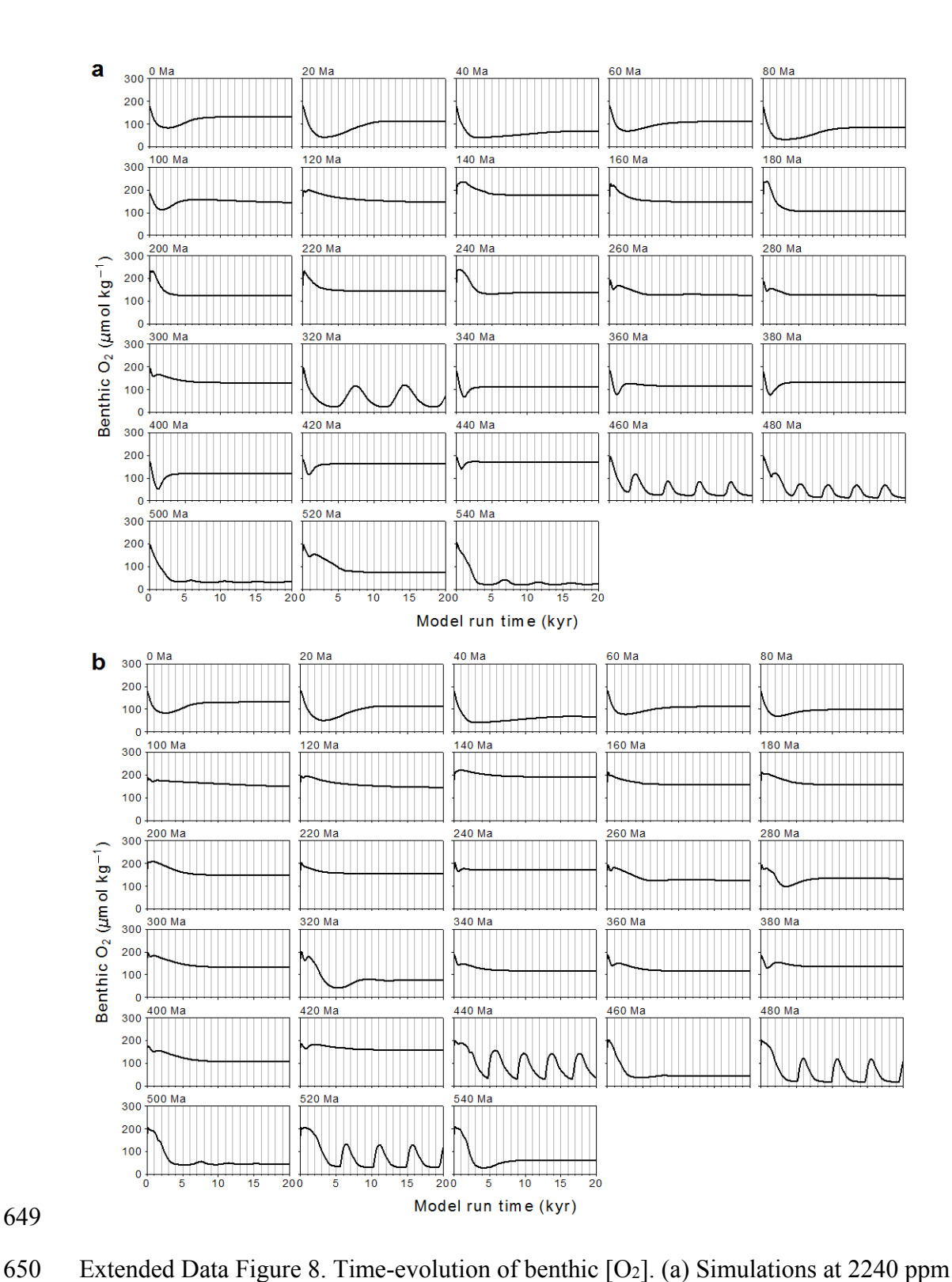
Extended Data Fig. 5. Earth System Model results for simulations at 2240 ppm CO₂ (like #1) but with no dependence of remineralization on temperature. (a) Same as Fig. 1. (b) Same as Fig. 2.



Extended Data Figure 6. Benthic oxygen concentrations for simulations at 2240 ppm CO₂ (like #1) but with no mid-ocean ridges (see Extended Data Fig. 7). Results are averaged over the last 5000 years. Emerged continental masses are shaded white. Eckert IV projection.



Extended Data Fig. 7: Bathymetry with mid-ocean ridges used in series #1 and #2 (a), and flat-bottomed bathymetric reconstructions used in simulations with no mid-ocean ridges (b) (see Extended Data Fig. 6). Only reconstructions for 0 to 140 Ma (both included) differ (see Methods). Emerged continental masses are shaded white. Eckert IV projection.

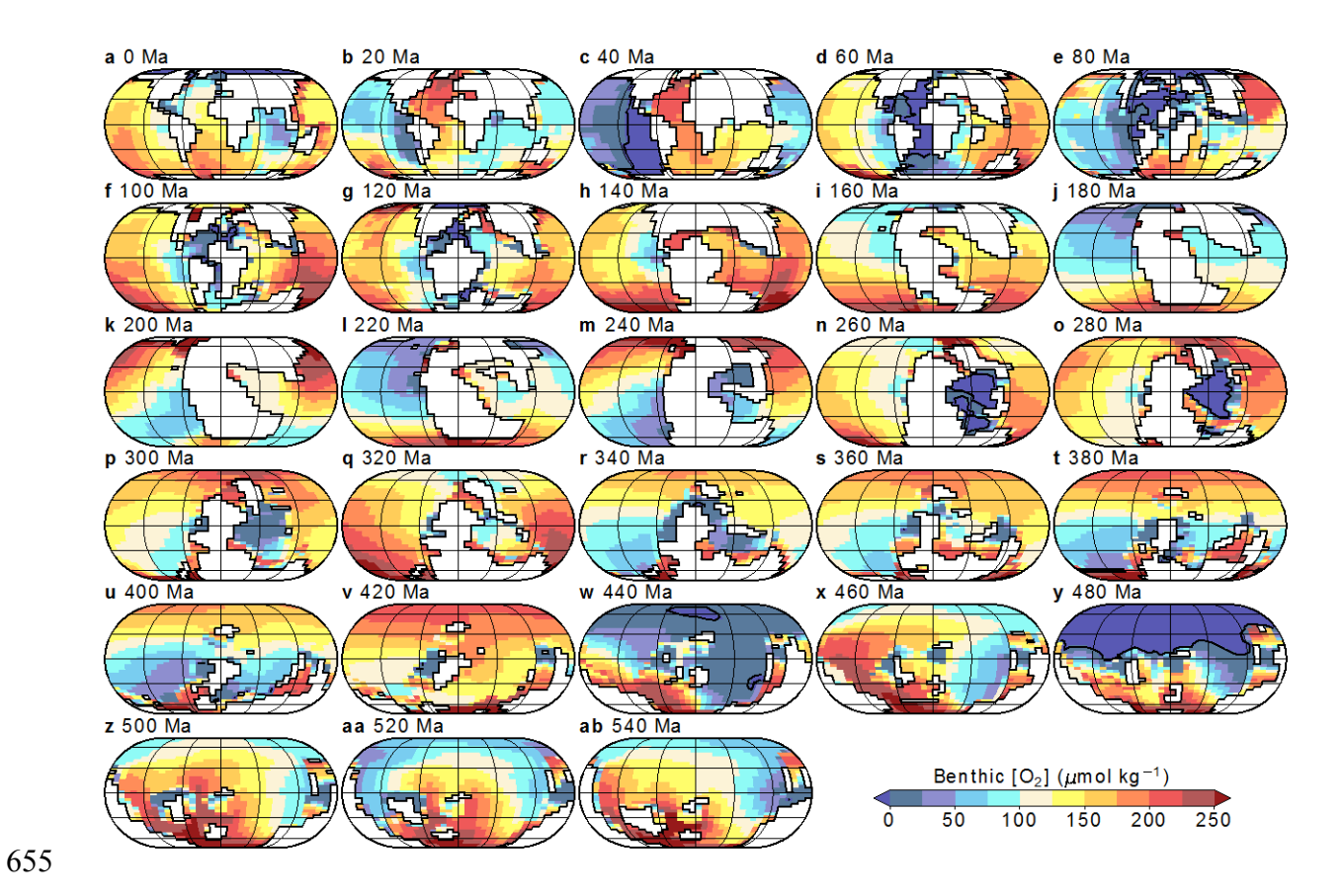


Extended Data Figure 8. Time-evolution of benthic [O₂]. (a) Simulations at 2240 ppm CO₂ with temperature-dependent remineralization (series #1). (b) Simulations in which we varied pCO₂ in order to approximately 'correct' for the paleogeographical impacts on climate (series #2).

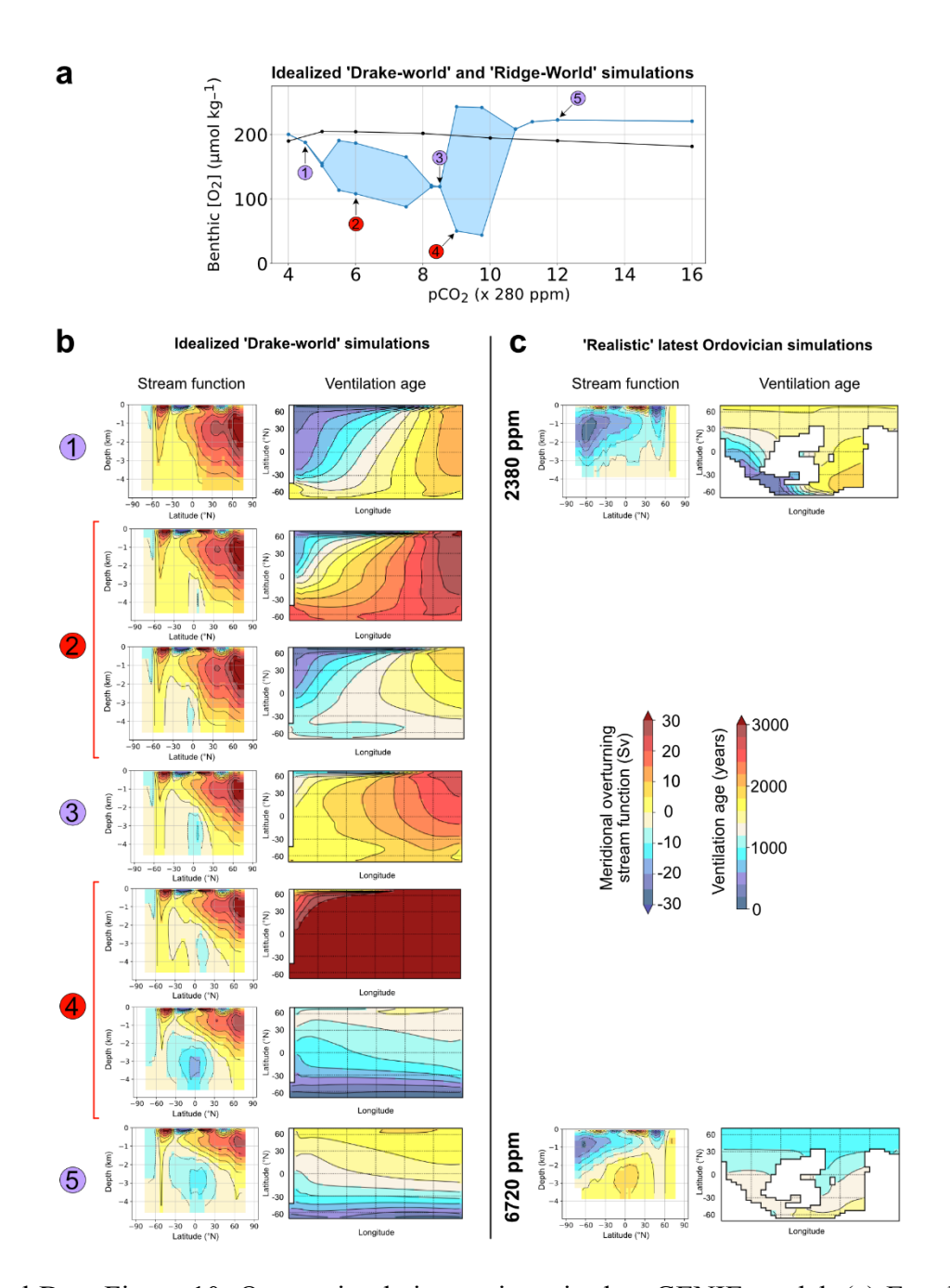
651

652

653



Extended Data Figure 9. Benthic oxygen concentrations for simulations at 1120 ppm CO₂, with temperature-dependent remineralization and mid-ocean ridges. Emerged continental masses are shaded white. Results are averaged over the last 5000 years. Eckert IV projection.



Extended Data Figure 10: Ocean circulation regimes in the cGENIE model. (a) Envelope of benthic $[O_2]$ values simulated at various atmospheric CO_2 levels using Drake world (in blue, see maps in panel (b)) and ridge world (in black) (Methods). Regimes of stable equilibria and regimes of stable oscillations for Drake World simulations are numbered and labelled using a blue and red background, respectively. (b) Meridional overturning stream function in Sv (sverdrup, 1 Sv = 10^6 m³ s⁻¹) and map of benthic ventilation age for each stable equilibrium and the 2 extreme states of each stable oscillatory regime identified in panel (a), using same

numbering and color code. Lambert cylindrical equal-area projection. A negative (blue) stream function corresponds to an anticlockwise circulation. (c) Tentative comparison with the latest Ordovician simulations of Pohl et al.²¹. Results are shown at 6720 ppm and 2380 ppm CO₂, corresponding to the warm and cold states of Scenario #1 in ref.²¹.